Journal of Power Sources 365 (2017) 210–219

Contents lists available at ScienceDirect

Journal of Power Sources

journal homepage: www.elsevier.com/locate/jpowsour

Correlation between triple phase boundary and the microstructure of Solid Oxide Fuel Cell anodes: The role of composition, porosity and Ni densification

Xuekun Lu [a], Thomas M.M. Heenan [a], Josh J. Bailey [a], Tao Li [b], Kang Li [b], Daniel J.L. Brett [a], Paul R. Shearing [a, *]

[a] Electrochemical Innovation Lab, Department of Chemical Engineering, University College London, London, WC1E 7JE, UK
[b] Department of Chemical Engineering, Imperial College London, London, SW7 2AZ, UK

HIGHLIGHTS

- An active TPB quantification algorithm for 3D reconstructed volumes is proposed.
- Sharp TPB density change occurs below percolation threshold of pore and Ni.
- Balanced surface area ratio of three phases is critical in optimizing TPB density.
- Mitigated Ni densification during sintering can improve TPB density by 70%.
- TPB is limited by Ni/YSZ connection and interfacial area at high porosity (>25%).

GRAPHICAL ABSTRACT

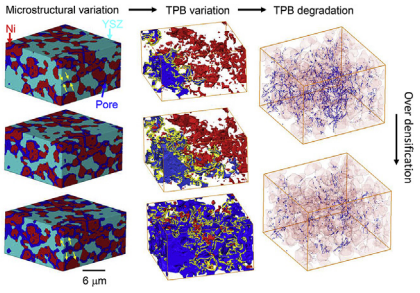

ARTICLE INFO

Article history:
Received 7 June 2017
Received in revised form
23 August 2017
Accepted 25 August 2017

Keywords:
X-ray tomography
Ni sintering
Electrode composition
Porosity
TPB degradation
Particle network

ABSTRACT

This study aims to correlate the active triple phase boundaries (TPBs) to the variation of as-prepared anode microstructures and Ni densifications based on the reconstructed 3D volume of an SOFC anode, providing a point of comparison with theoretical studies that reveal the relationship of TPBs and the material microstructure using randomly packed spheres models. The TPB degradation mechanisms are explained using a particle network model. The results indicate that in low porosity regime, the TPBs sharply increase with the porosity until the percolation threshold (10%); at intermediate porosity (10%–25%), a balance of surface area between three phases is more critical than that of volume fraction to reach the optimal TPB density; in the high porosity regime (>25%), the TPBs start to drop due to the shrinkage and detachment of Ni/YSZ interfaces. The TPB density is inversely proportional to the degree of Ni densification as long as the Ni content is above the percolation threshold (35%) and can be improved by 70% within 7% change of porosity provided that the over-densification is mitigated. This has implications for the design of SOFC microstructures as well for electrode durability, where Ni agglomeration is known to deleteriously impact long-term operation.

* Corresponding author.
E-mail address: p.shearing@ucl.ac.uk (P.R. Shearing).

http://dx.doi.org/10.1016/j.jpowsour.2017.08.095
0378-7753/

1. Introduction

Solid Oxide Fuel Cells (SOFCs) are one of the most promising electrochemical devices for the efficient co-generation of heat and electricity operating on a range of fuel gases [1,2]. SOFCs are composed of an electrolyte sandwiched between an anode and a cathode, the latter of which are fed with fuel gas and air respectively. Porous Ni-YSZ (8 mol% yttria-stabilized zirconia) is a state-of-art anode material for SOFC applications. The reaction at the anode/electrolyte interface couples the charge transfer of oxide ions in YSZ, electrons in Ni and the transport of fuels in the pores. The electrochemical reaction takes place at sites where the reaction constituents (i.e. ions, electrons and fuel gas) can simultaneously co-exist. Such reaction sites are called triple-phase boundaries (TPBs) [3,4], i.e. the boundary where the Ni, YSZ and pore phases meet. The rate of the chemical reaction is proportional to the TPB length, which is a function of particle size, distribution of the three phases and composition of the anode [5,6]. However, only those TPBs that belong to a percolating network of each transporting phases are considered to be active for the charge transfer reaction.

Quantification of active TPBs is a valuable metric for the determination of the optimal structure and composition that yields maximum electrochemical performance, as well as for coupling the anode degradation in terms of active TPB loss with the reduction in electrochemical performance. Previous studies have developed geometrical models to measure the TPBs in electrodes in which the solid phase is represented by spheres [1,7–9] from FIB-SEM data [10–13] or from X-ray nano-computed tomography (CT) [6].

With the fast development of X-ray CT, it is possible to routinely image the microstructure of the electrode at the voxel size of approx. 20 nm using a lab-based system. This enables the identification and segmentation of Ni/YSZ phases [14] and quantification of the TPBs degradation after anode degradation [15].

The theoretical study based on the randomly packed spheres model shows that, for spherical particles of equal particle size, the percolation threshold occurs between 30 and 35 vol% for the solid phases [16] and the maximum active TPBs lies between the percolation thresholds of the solid phases. The standard deviation of the particle size distribution is inversely proportional to maximum TPB lengths. The percolation and the TPB are more affected by larger particles than by smaller ones due to the surface-area to volume ratio [8]; as the particle size is reduced, the TPB density increases. However, this approach is limited by the use of spherical particles which do not represent the real microstructure, nor the distribution of the solid phases, nor the morphology of the pore phase in the anode.

Long-term durability is a key issue limiting the commercial application of SOFCs as the elevated operating temperature can result in electrode degradation after long-term operation [17,18]. Coarsening of Ni in the Ni-YSZ electrode has been identified as an important degradation mechanism as it gives rise to a decrease of TPB density [19,20]. Of course, the microstructure of the as-prepared anode material also has a significant impact on the initial performance as well as on the long-term stability. Ni-YSZ anode structures can vary greatly depending on initial Ni/YSZ ratio, porosity and particle size distribution, and sintering conditions amongst other processing parameters [21,22]. It is reported that increasing the ratio of Ni to YSZ increases the Ni coarsening rate as higher porosity and less YSZ lead to less obtrusive YSZ networks for Ni coarsening.

In the electrode fabrication processes, sintering plays an important role in the connectivity of the solid phases and porosity of the anode. Grain boundary diffusion removes the material from the surface of the particle at the grain boundary, which is relocated to particle necks, whilst broadly maintaining the particle shape. The fusion of the particle boundaries in terms of the expansion of the neck results in the densification of the composite powders [23]. The temperature required to activate sintering varies between materials but is generally proportional to melting temperature [24]. Thus Ni particles are considered to be more mobile than the YSZ particles.

Great effort has been made to link the ionic conductivity and strength of the YSZ electrolyte with the degree of densification [25–27], but few in the literature record the densification of the anode. Chen et al. [28] have studied the sintering behavior of Ni-YSZ and claims that smaller-sized Ni particles enhance the percolation network therefore less Ni is advantageous, leading to the mitigation of thermal expansion mismatch. However, there remains a lack of understanding of the relationship between densification of the as-prepared anode and the TPB density and the percolation of Ni.

The aim of this study is to unravel the complex relationship between the microstructure of the anode and the TPB density so as to understand the TPB degradation mechanisms. This is achieved using a combination of high-resolution X-ray CT and image analysis. Firstly, an algorithm for TPB density quantification is introduced in detail. Then, two theoretical studies are presented: 1) investigation of the TPB density as a function of the as-prepared anode with different initial compositions and global porosities; 2) investigation of the TPB density and Ni percolation as a function of the degree of densification in Ni-YSZ anode. The TPB degradation mechanisms will be analyzed in details for both studies to provide insights for the optimization of electrode fabrication and better electrochemical performance.

2. Materials and methodology

2.1. Materials

The anode was fabricated using a phase inversion technique [29–33]. Commercially available powders of yttria-stabilized zirconia (8YSZ, mean particle size 0.1–0.4 μm) and nickel oxide (NiO, mean particle size 0.5–1.5 μm) were purchased from Inframat Advanced Materials and used as supplied. Polyethersulfone (PESf) (Radal A300, Ameco Performance, USA), 30-dipolyhydroxystearate (Arlacel P135, Uniqema), and *N*-methyl-2-pyrrolidone (NMP, HPLC grade, VWR) were used as the polymer binder, dispersant, and solvent, respectively. A suspension composed of ceramic particles (60% wt. NiO), solvent and polymer binder were mixed for 3–4 days via planetary ball milling (SFM-1 Desk-top Miller, MTI Corporation, USA) to assure homogeneity, and were subsequently degassed under vacuum to fully eliminate air bubbles trapped inside. The composite compact powder was then sintered at 1200 °C for 6 h, followed by the reduction at 700 °C for 2.5 h in pure H_2.

2.2. X-ray Computed Tomography (X-ray CT)

The anode was imaged in 3D using an Ultra 810 X-ray microscope (Carl Zeiss XRM, CA, USA) [34]. This machine produces a 5.4 keV quasi-monochromatic parallel beam, and can achieve sub 100 nm voxel resolutions by the use of X-ray optics. A small piece of sample was manually extracted from the anode in order to obtain a cylindrical imaged volume with approx. 20 μm diameter, giving a voxel size of 64 nm. The spatial solution is measured to be 85 nm using the same Au resolution test pattern as was reported previously [35]. A projection was collected every 40 s using a 1024 × 1024 pixel 16-bit camera under binning 4 mode. Each projection was separated by an angle of 0.15°. This resulted in 1201 projections over a 180° scan, which was then reconstructed by a standard filtered-back projection algorithm in the Zeiss XMReconstructor software. A sub-volume of 10 × 10 × 6.5 μm^3 was

extracted from the reconstructed volume and subsequently imported into the image processing software Avizo 9.0 (FEI, Bordeaux, France) for phase segmentation using a watershed algorithm [36]. A representative volume analysis was conducted to verify the extent to which the volume can be considered representative of the material in general. The metrics of the pore phase (i.e. porosity and tortuosity factor) were investigated. Results show that the porosity and the tortuosity factor converge at 70% and 60% of the sample volume studied, corresponding to the sample volume 390–450 μm^3, which proves the representativeness of the subsample selected for further analysis.

2.3. Active TPB measurement

TPBs can be calculated using geometrical methods based on mathematical models [1,7–9] and empirical methods [2], nevertheless, these TPBs are defined based on randomly packing spherical particles. In reality, it is a different case for the quantification of TPBs from FIB-SEM or X-ray CT data, in which the particles are voxelised into cubes with certain resolutions. An in-house algorithm developed in Matlab has been used in this study for active TPB quantification of a given 3D matrix which contains three segmented phases (i.e. red: Ni, cyan: YSZ and blue: pore in Fig. 1).

The algorithm operates as follows: 1) two opposite planes on the bounding box of the volume are assigned as the electrode/electrolyte interface and the current collector. The Ni and pore voxels which do not have a percolating path originating from the current collector and the YSZ voxels from the electrode/electrolyte interface will be removed according to their coordinates (i.e. the particles labelled with yellow crosses in Fig. 1a); 2) interstitial planes are inserted between every rows, columns and vertical slices to generate candidate vacancies for TPB points (Fig. 1b and c); 3) identification of the TPB points by checking the 3×3 neighborhood voxels centered at every vacancy points. As long as at least one set of Ni + YSZ + Pore voxels is included, the target vacancy will be identified as a TPB point; 4) a calculation matrix (Fig. 1e) which represents the Euclidian distance will be superimposed on each of the identified TPB points (yellow sphere in Fig. 1d) to conduct pointwise multiplication and summation. After dividing it by two (i.e. each pair of TPB points is counted twice), the final TPB length can be obtained.

2.4. Microstructure manipulation for theoretical study

The parametric study based on the microstructure variation is achieved by morphological operations, which were previously reported to be applied to the 3D pore phase in gas diffusion layer in fuel cells [37]. For the purpose of investigating the TPB density as a function of the composition and porosity (ε) of the as-prepared anode the obtained CT data was used as a "seed" data set to generate a sequence of altered microstructures *in-silico*. Morphological operations (i.e. erosion and dilation) were conducted on the segmented YSZ phase from the reconstructed volume, while the volume fraction of Ni particles was maintained at the same value. This is conceptually the same idea used by researchers who simulated random packings of particles to study the dependence of effective properties by inflating the particle radius as the only controlled variable [38]. This method can avoid the errors and uncertainties introduced by using real samples sintered in different conditions, which would vary other several morphological properties at the same time. A spherical structuring element with varying sizes was used to control the strength of erosion/dilation so as to achieve microstructures of a range of porosities and Ni/YSZ volume fraction ratio. A detailed introduction of the morphological operations can be found elsewhere [39–41].

The densification process was mimicked by "opening" and "closing" operations on the Ni phase of the seed data. They are well-developed morphological operations both derived from the fundamental operations of erosion and dilation but with more control over the affected features: erosion/dilation simply shrink/grow the boundaries of the particles isotropically while opening/closing only operates on the features which are smaller than the

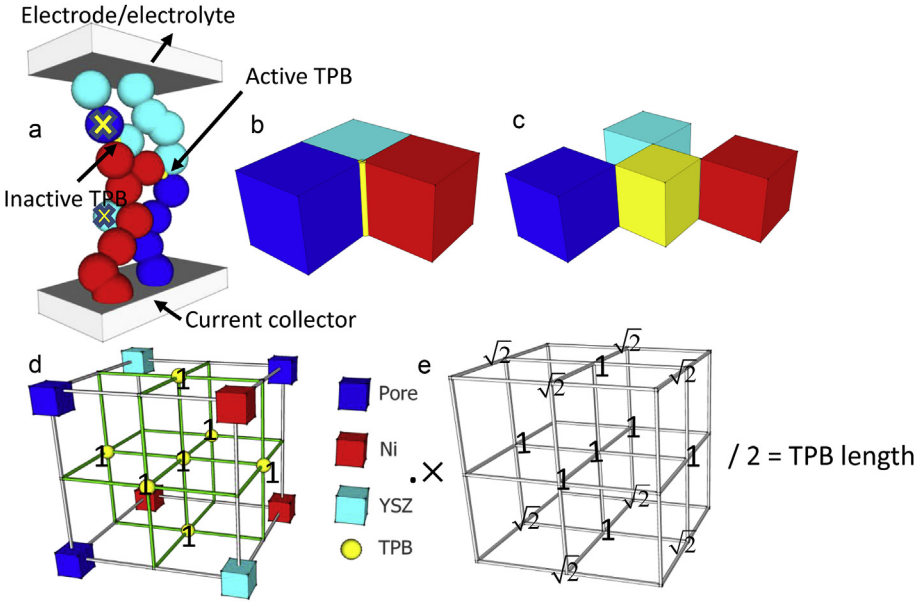

Fig. 1. Schematic of the algorithm of active TPB quantification. (a) illustration of percolating network and active/inactive TPBs. The non-percolating particles labelled using yellow crosses are to be removed; (b)–(c) expansion of adjacent three phases by inserting interstitial lattice points to create candidate vacancies of the TPBs (yellow); (d) An example of a possible arrangement of TPBs according to the position of the surrounding three phases; (e) the calculation matrix with the numbers indicating the Euclidian distance relative to the centre node. By superimposing the center node of this matrix on each of the TPB points (represented as 1 in (d)) and performing multiplication and summing up, the TPBs length can be measured. (For interpretation of the references to colour in this figure legend, the reader is referred to the web version of this article.)

spherical structure element [41,42]. The different degrees of densification were achieved by varying the diameter of the structural element from 1 to 3 voxels which represent the maximum diameter of the pore throat to be filled by Ni coalescence. Fig. 2a shows a 2D ortho-slice of the original microstructure of the segmented anode (red: Ni, blue: pore, cyan: YSZ). The pixels modified by dilation/erosion operation at YSZ/pore boundaries are marked in white (Fig. 2b). By using opening/closing operation, the pore phases which are smaller than the structuring element (yellow circle 1) in the initial microstructure (Fig. 2a) will be replaced by Ni pixels while those larger than the structure element will be kept (yellow circle 2). Consequently, the white pixels in Fig. 2c indicate the newly formed Ni pixels. These operations effectively imitate the densification process in terms of decreasing particle surface curvature, internal homogenization and neck growth, as is pointed out by the yellow arrows. It needs to mention that this parametric study focuses on the TPB density as a function of local densification of Ni particles while maintaining the macroscopic morphology. As a consequence, the volume fraction of Ni is not a constant thereby showing volume changes from 1% to 9% depending on the degree of densification.

3. Results and discussion

3.1. Microstructure of the original anode

A virtual ortho-slice of the reconstructed 3D volume of the anode is shown in Fig. 3a. Three phases can be clearly distinguished from the good contrast of the grayscale values. Porous Ni particles are observed. Fig. 3b shows the result of watershed segmentation of the three phases. It is noted that Ni particles demonstrate clear boundaries and each individual particles is distinguishable. In contrast, the YSZ phase is dense and the grain boundaries are fused together, resulting in a larger particle size. This discrepancy is proposed to originate from the reduction of NiO and the resultant volume shrinkage of Ni [43,44]. Fig. 3c is the skeleton of the pore network, from which it is found that the average size of the pore phase is 230 ± 41 nm. Fig. 3d shows the arrangement of the TPBs (yellow lines) relative to the Ni (red) and pore (blue) phase. The microstructural parameters of the as-prepared anode are measured by CT data and shown in Table 1, compared with the parameters from global measurements (i.e. bulk material property, labelled with asterisks). The porosity of the bulk sample is measured by a laboratory fluid-saturation method [45] and the densities are deducted from the composition. It is found that the measured Ni and YSZ volume fractions are consistent with the theoretically calculated value [46]. The porosity measured from the bulk material is slightly higher than the CT method, which could be resulted from the tiny internal pores in the Ni particle below CT resolution but were captured by the fluid, but this type of pores does not contribute to TPBs.

3.2. Parametric study 1: TPB vs. Microstructures

The morphological operations (i.e. dilation and erosion) on the YSZ phase render a series of samples with different Ni/YSZ volume fraction ratios and global porosities, while the Ni phase morphology and volume fraction were maintained constant. Fig. 3e and f shows the dilated and eroded microstructure from the seed data (Fig. 3b). The distribution of active TPBs as a function of

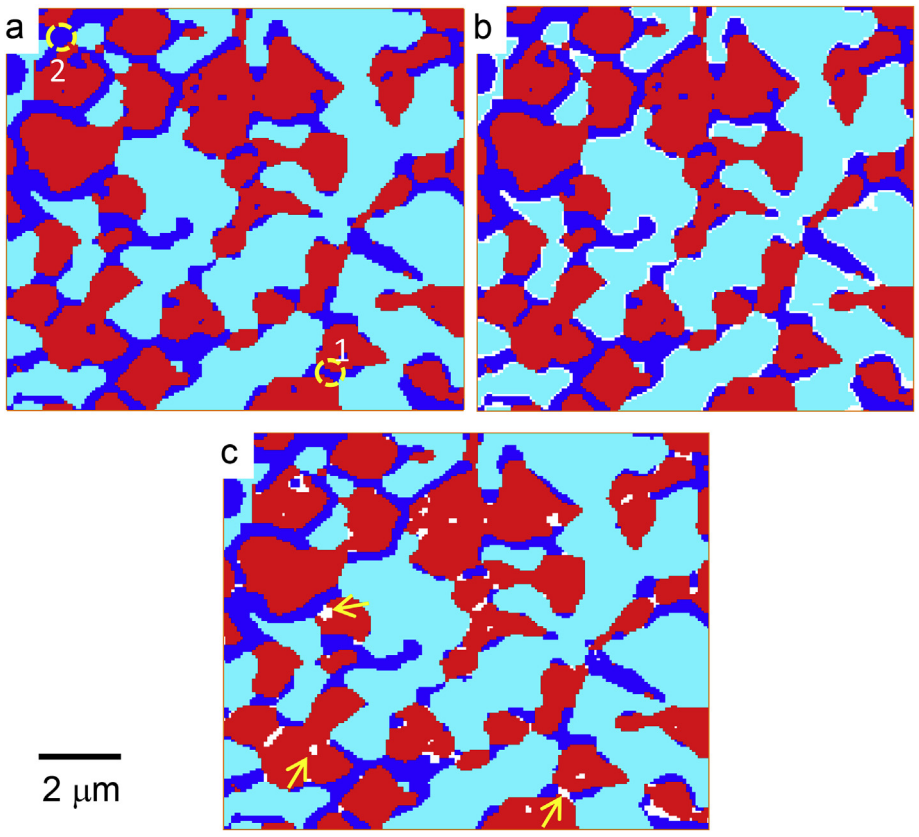

Fig. 2. Illustration of the microstructure manipulation using morphological operations. (a) The original microstructure of the anode; (b) the pixels modified by the dilation/erosion operations at YSZ/pore boundary are marked out in white colour; (c) densification process is imitated by opening/closing operation. The pores that are smaller than the structure element in (a) are changed into Ni while the ones larger than structure element are kept.

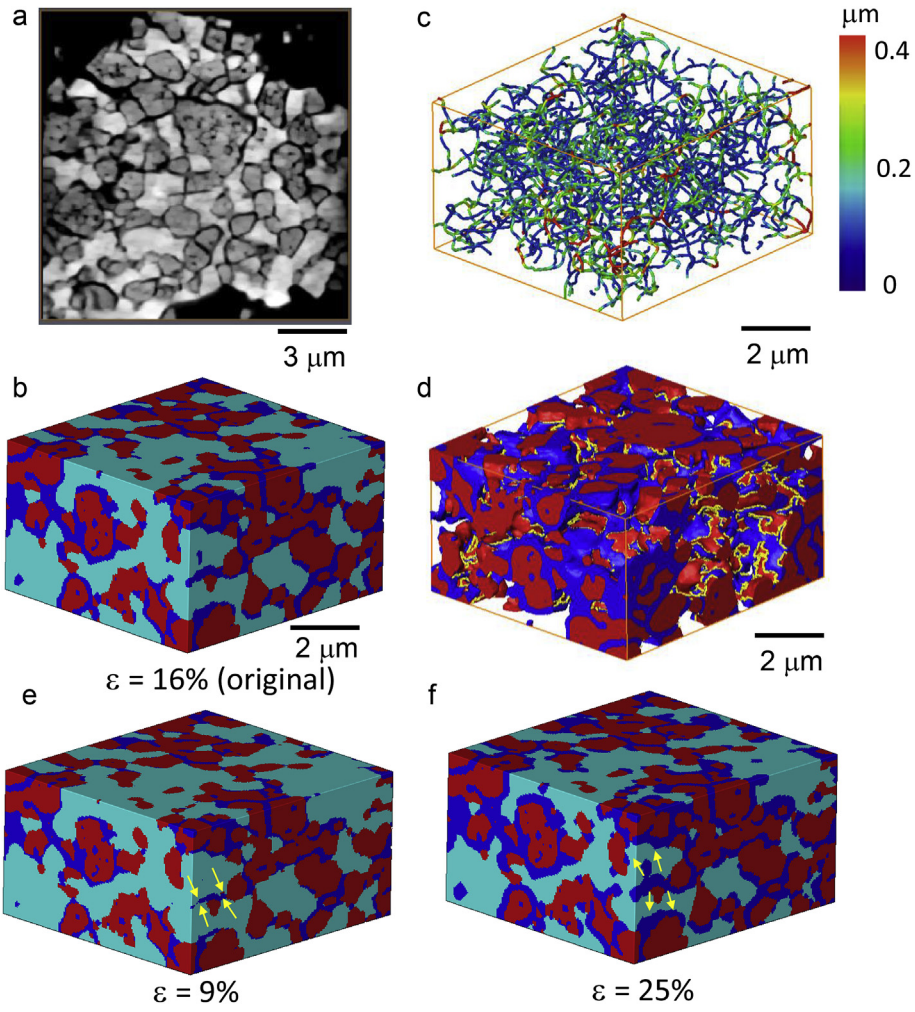

Fig. 3. (a) A virtual orthoslice of the reconstructed 3D volume (Ni: dark gray, YSZ: light gray, pore: black); (b) three phases are segmented using watershed method (red: Ni, cyan: YSZ, blue: pore); (c) skeleton of the pore network, with colourmap showing the diameter distribution; (d) TPBs arrangement (yellow lines) relative to the Ni and pore phase; (e)–(f) resultant microstructures after morphological operations on the YSZ phase, rendering microstructures with varying YSZ particle sizes, Ni/YSZ ratios and porosities; (e) dilation once from seed data shown in (b); (f) erosion once from (b). Yellow arrows show the morphological change of the pore phase. (For interpretation of the references to colour in this figure legend, the reader is referred to the web version of this article.)

Table 1
Material parameters of the anode before and after the reduction (variations between four measured samples are shown by STD).

	Dimension (μm)	Volume fraction (%)	Porosity (%)	Density ($g \cdot cm^{-3}$)	TPB (μm^{-2})
NiO	0.1–0.4*	54.2 ± 0.6*	3.2 ± 0.3*		
YSZ	0.5–1.5*	42.5 ± 0.9*		6.1 ± 0.1	
Ni	0.66 ± 0.15	37.1 ± 3.5		5.7 ± 0.4	6.4 ± 0.51
YSZ	1.1 ± 0.17	46.5 ± 2.7			
Pore	0.23 ± 0.04	16.2 ± 1.6	18.1 ± 0.4*		

porosities is visualized in Fig. 4. The percolated and non-percolated pores are labelled as blue and red, respectively. It is found that at low porosity, the percolated TPB distribution is limited to only one-third of the distance from the percolation side. With the increase of porosity (i.e. erosion of the YSZ), the merging of the percolated and non-percolated pore phase leads to the increase of the total active TPB length. The magnitude of the active TPB density as a function of the porosity is plotted in Fig. 4e.

It is found that the TPB density experiences an initial increase when the porosity is below 9%, then maintains stable at a plateau at 6.5 μm^{-2}, followed by a decrease when the porosity exceeds 25%. The plot of percolation ratio against porosity indicates that the percolation of the pores greatly affects the TPB density when the porosity is below 9%, which is a bottleneck value of global percolation. After this point, the TPB density is less dependent on the porosity and pore phase percolation. Our study is consistent with the literature [16] which says that the percentage of the percolated pores is above 99% when the porosity $\varepsilon > 25\%$. However, the loss of the TPB density at the high porosity regime is unexpected and will be discussed later.

The graphs in Fig. 4e also compare the volume fraction and surface area fraction of each individual phase at different porosities. It is already known that the sharp increase of the TPB curve is due to the percolation of the pores, and by comparing the two column

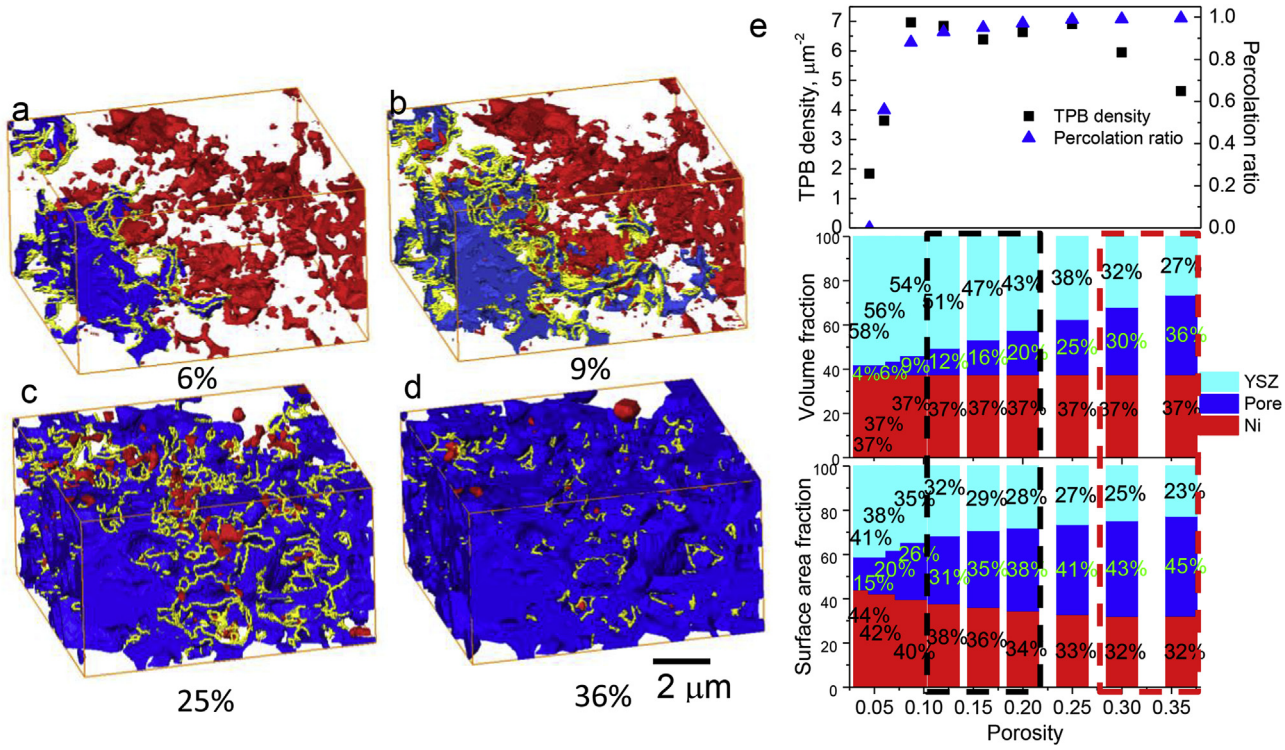

Fig. 4. (a)–(d) Distribution of active TPBs (yellow lines) as a function of porosity. The percolated and non-percolated pores are labelled as blue and red, respectively; (e) TPB density and percolation ratio are plotted as a function of anode with different compositions. The dataset with $\varepsilon = 16\%$ corresponds to the original sample. (For interpretation of the references to colour in this figure legend, the reader is referred to the web version of this article.)

graphs at the plateau regime, it is noted that there is a large difference in volume fraction of the three phases but similar surface area fraction (marked by dashed black lines). When the TPB density starts to drop ($\varepsilon > 30\%$), the ratio of the volume fraction of the three phases is more uniform compared to that of the surface area fraction (marked by dashed red lines).

Using a randomly packed spheres model, Abbaspour et al. [7] and Kenney et al. [8] stated that the peak of the TPB density is reached when the volume fraction of the Ni is equal to YSZ when they have the same mono-sized particles. However, a larger Ni or YSZ particle will shift the peak of TPB density toward higher volume fraction of Ni or YSZ due to a change of Ni or YSZ percolation threshold. Although this is consistent with what we observe here: the peak of TPB density shifts from 50:50 Ni/YSZ to the higher YSZ volume fraction, it is of great interest to examine if the percolation threshold of YSZ phase is the right or only contribution to the high TPB. Accordingly, the TPB degradation mechanism is inspected in the next section to decouple the contribution from global metric (solid phase percolation) with the contribution from microstructure characteristics.

TPBs at different porosities are superimposed onto one another as is shown in Fig. 5a. TPBs increase by 300% with increasing porosity from 5% to 16% but decrease by 30% at a porosity of 36%. The visualization of the TPBs clearly shows that there is no macroscopic loss of the TPBs when the composition (YSZ: Pore: Ni) changes from 47%: 16%: 37%–27%: 36%: 37%, which implies that the percolation of YSZ is not a reason for TPB loss in this case. However, it is noted that some of the TPBs disappear at local places compared with the 16% porosity sample. Thus, a region of interest (ROI) analysis was conducted on the small volume indicated by the red box (Fig. 5a). The slice of ROI in Fig. 5b shows that the increase of the porosity from 16% to 36% leads to shrinkage of the contacting Ni/YSZ area, even detaching the contacted Ni/YSZ faces. The yellow

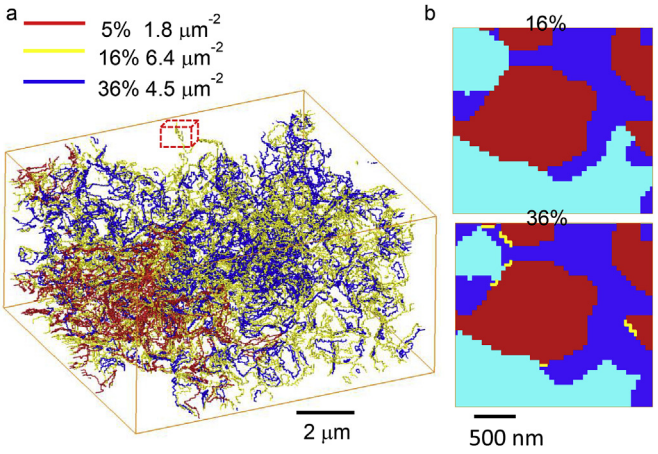

Fig. 5. Region of interest investigation of the TPB degradation mechanism. (a) Superimposition of the TPBs of $\varepsilon = 5\%$, $\varepsilon = 16\%$ and $\varepsilon = 36\%$ sample. The loss of TPB from 16% to 36% is indicated by the red box; (b) slices from the red box in (a) indicate the shrinkage and detachment of the contacting faces between Ni/YSZ. Yellow lines represent the lost TPBs. (For interpretation of the references to colour in this figure legend, the reader is referred to the web version of this article.)

lines represent the diminished TPBs from $\varepsilon = 16\%$ to $\varepsilon = 36\%$. In a real sample, geometrical changes of this nature could reflect the resultant microstructure originating from 16% porosity sample due to a lower uni-axial pressure applied on the pellet, higher volume fraction of pore former or a lower sintering temperature/time.

The qualitative analyses show the decrease of contacting area by shrinkage and detachment causes the TPBs degradation. Further analysis was conducted to quantify this effect as a function of different compositions. To do so, a particle network model (PNM)

was used, in which the particles were modeled as spheres that sit at the mass centre of the particles. The sizes of the spheres are proportional to the real size of the particles, as is shown in Fig. 6a. The local thickness distribution [47] between each pair of Ni/YSZ particles was measured and visualized as a yellow tube in Fig. 6b. The diameter of the tube is proportional to the varying thickness. In the shown particle pair, the throat appears to be the minimum of the local thickness. Fig. 6c shows the application of this model to the whole anode and the network of the Ni/YSZ is clearly seen. It depicts that due to the much larger size, each YSZ particle is contacted by multiple Ni particles.

The quantification result of the PNM (Fig. 6d) shows that with the increase of porosity from 5% to 36%, the average Ni/YSZ interfacial area decreases from 1.28 μm^2 to 0.25 μm^2, and the total pairs of connected Ni/YSZ particles drop by 30%. It is noted that unlike the interfacial area, the paired particle number remains stable when the porosity is below 12%, after which it starts to drop at a gentle rate, and then drastically decreases after $\varepsilon = 25\%$.

As a summary, the TPB density is determined by a variety of limiting factors at different porosity regimes. In the low porosity regime, the percolation of pores is the key factor limiting the TPB density [38,48], which increases at the same pace as the percolation ratio of the pores. At intermediate porosity levels (from 12% to 25%), the TPB density remains stable and is only marginally by the drop in the number of contacted Ni/YSZ pairs, instead, a balance of the surface area between three phases is the critical factor holding the TPBs at a high level. Indeed, the percolation of pore phase has little effect since the percolation ratio is above 95%. At high porosity levels (ε >25%), the coincidence of the turning point on the TPB density in Fig. 4e and the total paired particle number in Fig. 6d proves that the balance between Ni/YSZ/pore is broken and an abrupt and dramatic detachment of the Ni/YSZ pairs occurs, which outweighs any effect from the microstructure, leading to the decrease of the TPB density. No evidence of percolation limitation is found.

3.3. Parametric study 2: TPB vs Densification

Different degrees of densification were mimicked by morphological operations on the Ni/pore phase with the YSZ phase maintained constant, and the resultant microstructures are seen in Fig. 7. The disconnected Ni particles in the original microstructure (identified by yellow arrows, Fig. 7b) are connected after densification (Fig. 7a) but further apart in a lower degree of densification (Fig. 7c). The dependence of TPB density and Ni percolation on densification degree is plotted in Fig. 8a. It is found that the TPB is inversely proportional to the densification. Moreover, the peak value of the TPB density is 8.3 μm^{-2} at $\varepsilon = 18\%$, which is about 30% higher than that in the composition study in Section 3.2. This means the original microstructure ($\varepsilon = 16\%$) is over-sintered and could be tailored for the optimal TPB density. For an over-sintered microstructure, global modification of the porosity and composition doesn't remarkably increase the TPB density as is shown in Fig. 4e, instead, better control of the densification process can significantly benefit the TPB density by up to 70% within 7% change of the porosity. Similar to the previous study, the TPB density finally drops as the porosity goes higher, however, it occurs much earlier in the densification process, which can be accounted for by the

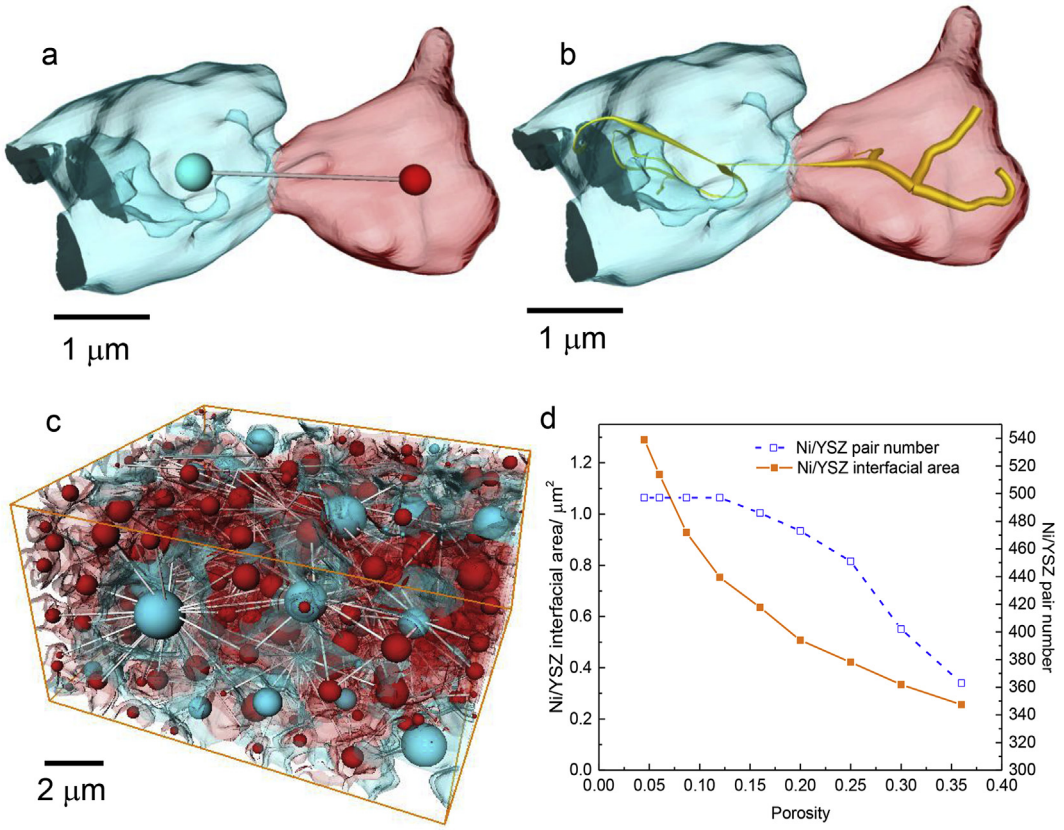

Fig. 6. Particle network model (PNM) established on the anode microstructure. (a) Particles are modeled as spheres sitting at the mass centre, with the diameter representing the particle size; (b) local thickness distribution is measured and visualized as a yellow tube, the diameter of which is proportional to the local thickness; (c) the application of particle network model to the whole anode obtained from nano-CT measurements; (d) the result of PNM measurement, showing the Ni/YSZ interfacial area and paired Ni/YSZ number as a function of the porosity. (For interpretation of the references to colour in this figure legend, the reader is referred to the web version of this article.)

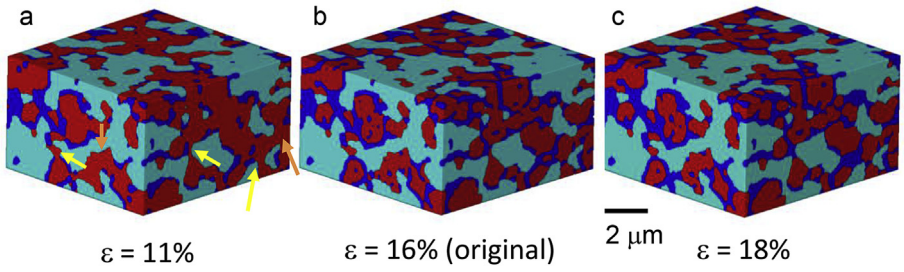

Fig. 7. Microstructure variation of different degrees of densification mimicked by image processing technique. The disconnected Ni particles pointed out by yellow arrows in the original sample (b) are connected after densification (a) and further apart with a lower degree of densification (c). The YSZ phase is maintained constant during the process. The yellow and orange arrows point out Ni particles coalescence and surface curvature smoothing respectively. (For interpretation of the references to colour in this figure legend, the reader is referred to the web version of this article.)

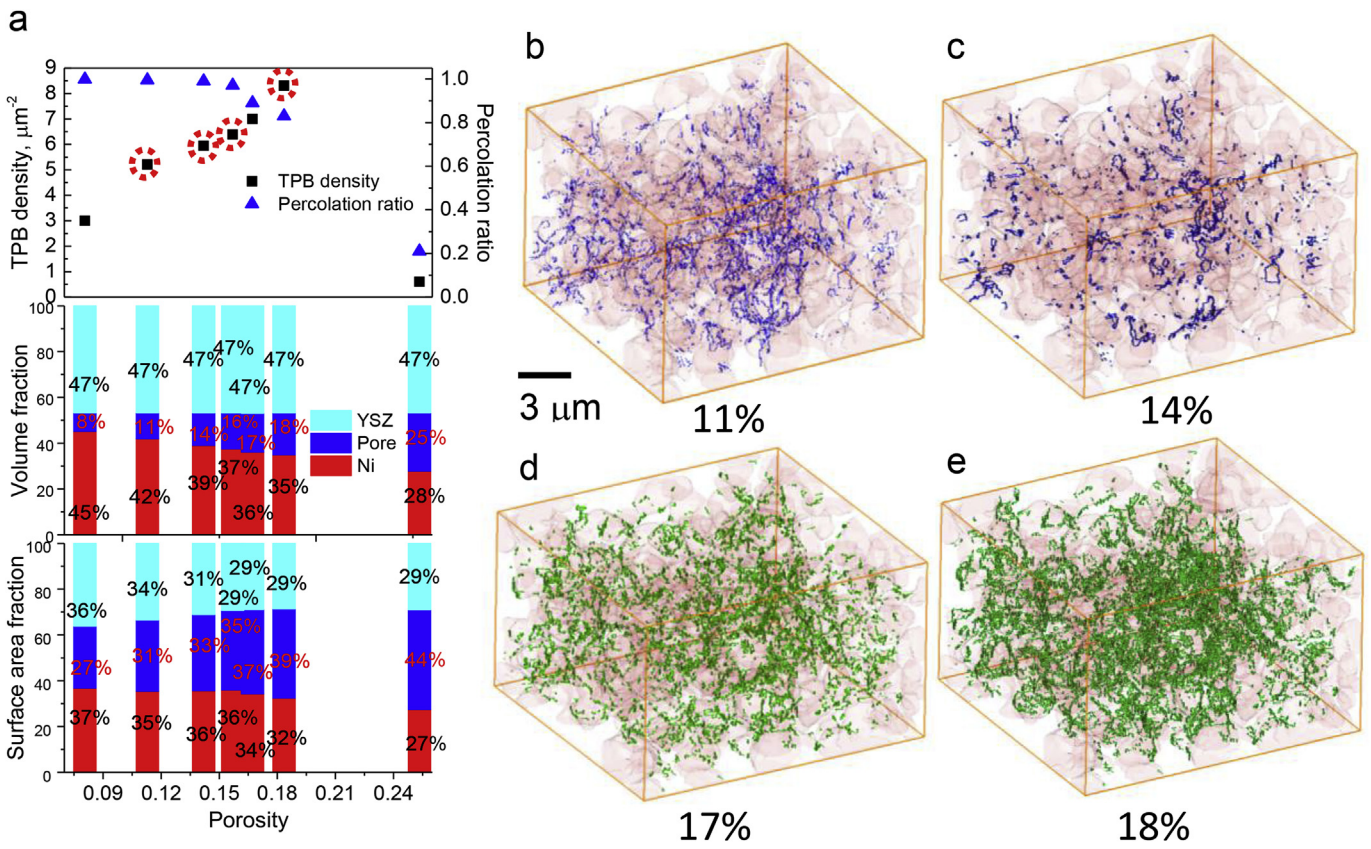

Fig. 8. (a) TPB density and Ni percolation ratio are plotted as a function of porosity in the densification process, alongside the corresponding volume fraction and surface area fraction. ε = 16% corresponds to the original sample. The change of TPBs relative to the original sample (ε = 16%) in the circumstance of (b)–(c) further densification and (d)–(e) lower densification. The blue and green lines mark the diminished and increased TPBs respectively. The Ni particles are shown as semi-transparent phase (red). (For interpretation of the references to colour in this figure legend, the reader is referred to the web version of this article.)

percolation ratio of Ni particles: only 20% of the total Ni are percolated when densified to ε = 25%, leading to the significant loss of TPB density. It is seen that the majority of the Ni are percolated from the Ni volume fraction of 36%, which is consistent with the literature saying the percolation threshold of Ni is between 30% and 40% [16,49,50].

Fig. 8b–e displays the change of TPBs map relative to the original sample under different degrees of densification. The blue lines in Fig. 8b and c indicate the loss of TPBs with further densification from ε = 16% whereas the yellow lines in Fig. 8d and e shows the increase of TPBs compared to the original sample if the sample is less densified. These four microstructures correspond to the four porosities marked as red circles in Fig. 8a. As is known, the majority of the free energy of a powder compact is associated with its surface energy, the primary driving force for sintering is the reduction of the internal surface area in terms of neck growth to smooth the variation in curvature of the particles. This is shown by the orange arrows in Fig. 7. However a thermodynamically favorable microstructure doesn't necessarily correspond to a kinetically favorable one. As is seen at the sites pointed out by the orange arrows, a high degree of densification removes active TPBs [23].

By comparing the TPB relationship with the as-prepared anode at different global porosities in Section 3.2 and different degrees of densification in this section, distinct difference in TPB degradation mechanisms are found for two cases: the former mainly comes from the loss of pairing Ni/YSZ interface when the global porosity

level is too high and in the low porosity regime, it is limited by the percolation of the pore phase. In contrast, the TPB loss in the densification process either comes from the over-densification which removes the active TPBs for a more thermodynamically stable system or from insufficient densification, causing a poorly percolated network of Ni phase. At low porosity regimes of the two studies, the TPB density is related to the percolation of pore phase. The upper limit of porosity for the optimal TPB distribution varies between the two cases because all the change of porosity in the densification process directly affects the connectivity of the neighboring Ni particles. The optimal porosity of the densification process may vary between samples, but as long as the Ni percolation is ensured (35% volume fraction), more densification process is less necessary for both electronic conductivity and electrochemical kinetics.

From the results shown above, it is desirable to have a good control the Ni densification process. Adjusting the porosity of the anode from 10% to 50% can be achieved by using lower NiO/YSZ sintering temperature or time, or adding pore-former. However, such high porosity comes at the expense of TPB density and structural integrity in long-term operation. The densification process continues in the reduction step as well (i.e. Ni sintering or aging). The primary driving force for Ni sintering is the reduction of the total energy of the system in terms of reducing the surface area of the particles and thereby the particle curvature. Low temperature and low ramp rate render a surface diffusion-controlled sintering process, in which the degree of densification is lower than that controlled by grain boundary diffusion mechanism occurring at high temperature (over 1400 °C) and longer holding time [24]. Densification can also occur in the early stage of the reduction process. It was observed that the Ni and YSZ particles are either weakly bonded or partly detached, forming gaps at the Ni/YSZ boundaries when reduced at 400 and 600 °C. In contrast, reducing at 800 °C renders close contact between Ni and YSZ particles and a high-density microstructure [51]. This is explained by the fact that NiO − Ni transformation mechanisms dominate low temperature reduction processes (500 °C) whereas Ni sintering is more active during high-temperature reduction (1000 °C) [52]. Apart from temperature, the change of the porosity is also related to the duration of reduction: the porosity decreases by 30% when aging up to 2000 h at 1000 °C. It should be noted that substantial Ni evolution can occur from less than 50 h of reduction time as the highly non-equilibrated Ni particles reduced from NiO increase the system total energy and tend to re-organize [53]. Moreover particle growth is highly accelerated by the moisture of the reducing environment [44,54], which is detrimental to Ni percolation and TPBs density.

The dependence of TPB density on process parameters summarized in this parametric study is well correlated to experimental data from the literature. It has been found that long-term aging (700 h) of Ni at 1150 °C causes the active TPB density to drop from 1.5 to 0.5 μm^{-2}. The TPB density also drops by 70% when aging at 1200 °C for 500 h compared to the same time at 1000 °C [55]. In the same study, the surface area ratio of the three phases (Ni: YSZ: pore) changes from 30%: 40%: 30%–17%: 62%: 21%, where the TPB drops significantly. This is consistent with our parametric study. Moreover, a faster ramp rate (7.5 °C/min) is more effective in suppressing Ni sintering as the particle shape is more elongated compared to the rounded ones at a low ramping rate (2.5 °C/min): the former exhibited 10% lower TPB degradation [56]. This can be accounted for by our analysis in that over-sintered Ni leads to the decrease of pore sites which otherwise could contribute to the active TPB, (c.f. orange arrows in Fig. 7). Heenan et al. [6] proved by experiment that a uniform volume fraction (i.e. approximately one-third of each phase) only renders the TPB density of 2.1–3 μm^{-2}, far less than an unbalanced composition (5.6 μm^{-2}), e.g. Ni (40 vol%): YSZ (40 vol%): pore (20 vol%). As the porosity and volume fractions of the solid phases are all far above the percolation threshold (i.e. approx. 10% and 33% respectively), the difference of TPB density between the two cases could come from the interfacial area of Ni and YSZ particles, or the paired Ni/YSZ particles. In our study, the Ni/YSZ interfacial area at $\varepsilon = 20\%$ is approximately 2 times as large as that at $\varepsilon = 30\%$ (Fig. 6), which is in good agreement with the ratio of TPB density at these two porosities. Guan et al. [57] have also established the link of TPB density with Ni/YSZ interfacial area by comparing two type of samples.

4. Conclusion

This study introduced a TPB quantification algorithm to correlate the active TPB density to different as-prepared microstructures (i.e. compositions, global porosities) and degrees of Ni densification using the framework of a reconstructed 3D volume of SOFC anode obtained from an X-ray CT scan. Image processing techniques (i.e. morphological operations) on the as-prepared sample were used to theoretically mimic the variation of microstructures from a real original state. It is found that in the low porosity regime (below 10%), the TPB density is mainly determined by the percolation of the pore network: TPB density increases sharply with the porosity until reaching the percolation threshold of 10%. At intermediate porosity levels (10%–25%), a balance of surface area fractions between the three phases is critical to reach an optimal TPB density (approx. 7 μm^{-2}), rather than the uniformity of the volume fraction, which is important for the microstructures with identical particle sizes, based on the random packing spheres model. No evidence shows the adverse effect from YSZ percolation even below the reported percolation threshold. In the high porosity regime (above 25%), TPB density drops due to a shrinkage or detachment of the Ni/YSZ interfaces. The average interface area decreases from 1.28 μm^2 to 0.25 μm^2 from the porosity of 5%–36% and the total pairs of connected Ni/YSZ particles drop by 30%. The densification analysis indicates that better control of the densification process can improve the TPB density by 70% within 7% of porosity change. Over-densification removes the active TPBs as the curvature of the Ni particle surface is smoothed to reach a thermodynamically favorable system. The TPB density is inversely proportional to the degree of densification as long as the Ni content is above the percolation threshold (approx. 35%). These findings unravel the relationship between microstructure and TPB density, providing insights into SOFC electrode design: 1) the pristine composition of the cermet powder should have a biased volume fraction towards the solid phase of larger particles to reach a balanced surface area fraction, on the premise that the percolation threshold of the smaller particle is fulfilled; 2) over-densification of the electrode could be suppressed by a variety of process parameters, not only in the NiO/YSZ sintering step, but also in the reduction process (ramp rate, duration, temperature, atmosphere etc). This is also important for electrode durability, where Ni agglomeration is known to deleteriously impact long term operation.

Acknowledgement

The authors acknowledge the support from the EPSRC under grants EP/N032888/1, EP/P009050/1 and EP/M014045/1, Paul R Shearing acknowledges funding from the Royal Academy of Engineering.

References

[1] L. Schneider, C. Martin, Y. Bultel, L. Dessemond, D. Bouvard, Electrochim. Acta 52 (2007) 3190–3198.

[2] S. Yang, T. Chen, Y. Wang, Z. Peng, W.G. Wang, Int. J. Electrochem. Sci. 8 (2013) 2330–2344.
[3] J.D. Fehribach, R. O'Hayre, SIAM J. Appl. Math. 70 (2009) 510–530.
[4] R. O'Hayre, D.M. Barnett, F.B. Prinz, J. Electrochem. Soc. 152 (2005) A439–A444.
[5] W. Zhu, D. Ding, C. Xia, Electrochem. solid-state Lett. 11 (2008) B83–B86.
[6] T.M.M. Heenan, J.J. Bailey, X. Lu, J.B. Robinson, F. Iacoviello, D.P. Finegan, D.J.L. Brett, P.R. Shearing, Fuel Cells 17 (2017) 75–82.
[7] A. Ali, X. Wen, K. Nandakumar, J. Luo, K.T. Chuang, J. Power Sources 185 (2008) 961–966.
[8] B. Kenney, M. Valdmanis, C. Baker, J. Pharoah, K. Karan, J. Power Sources 189 (2009) 1051–1059.
[9] V.M. Janardhanan, V. Heuveline, O. Deutschmann, J. Power Sources 178 (2008) 368–372.
[10] P. Shearing, J. Golbert, R. Chater, N. Brandon, Chem. Eng. Sci. 64 (2009) 3928–3933.
[11] A. Bertei, E. Ruiz-Trejo, F. Tariq, V. Yufit, A. Atkinson, N.P. Brandon, Int. J. Hydrogen Energy 41 (2016) 22381–22393.
[12] J.R. Wilson, W. Kobsiriphat, R. Mendoza, H.-Y. Chen, J.M. Hiller, D.J. Miller, K. Thornton, P.W. Voorhees, S.B. Adler, S.A. Barnett, Nat. Mater 5 (2006) 541–544.
[13] Z. Jiao, N. Shikazono, Sci. Bull. 61 (2016) 1317–1323.
[14] P. Shearing, R. Bradley, J. Gelb, S. Lee, A. Atkinson, P. Withers, N. Brandon, Electrochem. Solid-State Lett. 14 (2011) B117–B120.
[15] O.M. Pecho, O. Stenzel, B. Iwanschitz, P. Gasser, M. Neumann, V. Schmidt, M. Prestat, T. Hocker, R.J. Flatt, L. Holzer, Materials 8 (2015) 5554–5585.
[16] D. Bouvard, F. Lange, Acta Metal. Mater. 39 (1991) 3083–3090.
[17] G. Brus, K. Miyoshi, H. Iwai, M. Saito, H. Yoshida, Int. J. Hydrogen Energy 40 (2015) 6927–6934.
[18] Z. Jiao, N. Shikazono, J. Electrochem. Soc. 162 (2015) F571–F578.
[19] P. Tanasini, M. Cannarozzo, P. Costamagna, A. Faes, J. Van Herle, A. Hessler-Wyser, C. Comninellis, Fuel Cells 9 (2009) 740–752.
[20] F. Abdeljawad, B. Völker, R. Davis, R.M. McMeeking, M. Haataja, J. Power Sources 250 (2014) 319–331.
[21] B.S. Prakash, S.S. Kumar, S. Aruna, Renew. Sustain. Energy Rev. 36 (2014) 149–179.
[22] L. Holzer, B. Iwanschitz, T. Hocker, B. Münch, M. Prestat, D. Wiedenmann, U. Vogt, P. Holtappels, J. Sfeir, A. Mai, J. Power Sources 196 (2011) 1279–1294.
[23] R. Clemmer, in: Mechanical Engineering, University of Waterloo, Canada, 2006.
[24] J.S. Reed, Principles of Ceramics Processing, J. Wiley & Sons, 1995.
[25] J.d.M. Furtado, C. da Silva, P. de Miranda, I. do Fundão, in: CBECiMat, 2010. Brasil.
[26] T. Suzuki, T. Yamaguchi, K. Hamamoto, H. Sumi, Y. Fujishiro, Rsc Adv. 1 (2011) 911–916.
[27] R.M. Batista, E.N. Muccillo, ECS Trans. 13 (2008) 47–54.
[28] Z. Chen, Y. Sakane, T. Tsurumaki, Y. Ayame, F. Fujita, in: 16th International Conference of Composite Materials, 2007, pp. 1–6.
[29] S.M. Jamil, M.H.D. Othman, M.A. Rahman, J. Jaafar, A.F. Ismail, K. Li, J. Eur. Ceram. Soc. 35 (2015) 1–22.
[30] K. Li, Ceramic Membranes for Separation and Reaction, John Wiley & Sons Ltd, Chichester, UK, 2007.
[31] T. Li, Z. Wu, K. Li, J. Power Sources 273 (2015) 999–1005.
[32] H. Strathmann, K. Kock, Desalination 21 (1977) 241–255.
[33] S. Liu, Ceram. Int. 29 (2003) 875–881.
[34] R. Schurch, S.M. Rowland, R.S. Bradley, P.J. Withers, IEEE Trans. Dielectr. Electr. Insul. 22 (2015) 709–719.
[35] A. Tkachuk, F. Duewer, H. Cui, M. Feser, S. Wang, W. Yun, Z. für Kristallogr. Mater. 222 (2007) 650–655.
[36] K. Parvati, P. Rao, M. Mariya Das, Discrete Dyn. Nat. Soc. 2008 (2009).
[37] P.P. Mukherjee, Q. Kang, C.-Y. Wang, Energy & Environ. Sci. 4 (2011) 346–369.
[38] J.M. Zalc, S.C. Reyes, E. Iglesia, Chem. Eng. Sci. 59 (2004) 2947–2960.
[39] K.H. Höhne, W.A. Hanson, J. Comput. Assist. Tomogr. 16 (1992) 285–294.
[40] M.L. Comer, E.J. Delp, image 1 (1999) 12–15.
[41] J.Y. Gil, R. Kimmel, IEEE Trans. Pattern Anal. Mach. Intell. 24 (2002) 1606–1617.
[42] R.M. Haralick, S.R. Sternberg, X. Zhuang, IEEE Trans. pattern Anal. Mach. Intell. (1987) 532–550.
[43] R. Hales, A.C. Hill, Corros. Sci. 12 (1972) 843–853.
[44] S.P. Jiang, J. Mater. Sci. 38 (2003) 3775–3782.
[45] L.M. Anovitz, D.R. Cole, Rev. Mineral. Geochem. 80 (2015) 61–164.
[46] D. Sarantaridis, A. Atkinson, Fuel Cells 7 (2007) 246–258.
[47] M. Doube, M.M. Kłosowski, I. Arganda-Carreras, F.P. Cordelières, R.P. Dougherty, J.S. Jackson, B. Schmid, J.R. Hutchinson, S.J. Shefelbine, Bone 47 (2010) 1076–1079.
[48] A. Bertei, B. Nucci, C. Nicolella, Chem. Eng. Sci. 101 (2013) 175–190.
[49] M. Pihlatie, Stability of Ni-YSZ Composites for Solid Oxide Fuel Cells during Reduction and Re-oxidation, VTT, 2010.
[50] N.Q. Minh, J. Am. Ceram. Soc. 76 (1993) 563–588.
[51] H. Monzón, M.A. Laguna-Bercero, Electrochim. Acta 221 (2016) 41–47.
[52] Z. Jiao, A. Ueno, Y. Suzuki, N. Shikazono, J. Power Sources 328 (2016) 377–384.
[53] D. Kennouche, Y.-c.K. Chen-Wiegart, J.S. Cronin, J. Wang, S.A. Barnett, J. Electrochem. Soc. 160 (2013) F1293–F1304.
[54] L. Holzer, B. Iwanschitz, T. Hocker, B. Münch, M. Prestat, D. Wiedenmann, U. Vogt, P. Holtappels, J. Sfeir, A. Mai, T. Graule, J. Power Sources 196 (2011) 1279–1294.
[55] D. Kennouche, Y.-c.K. Chen-Wiegart, C. Riscoe, J. Wang, S.A. Barnett, J. Power Sources 307 (2016) 604–612.
[56] M. Kubota, T. Okanishi, H. Muroyama, T. Matsui, K. Eguchi, J. Electrochem. Soc. 162 (2015) F380–F386.
[57] Y. Guan, W. Li, Y. Gong, G. Liu, X. Zhang, J. Chen, J. Gelb, W. Yun, Y. Xiong, Y. Tian, H. Wang, J. Power Sources 196 (2011) 1915–1919.